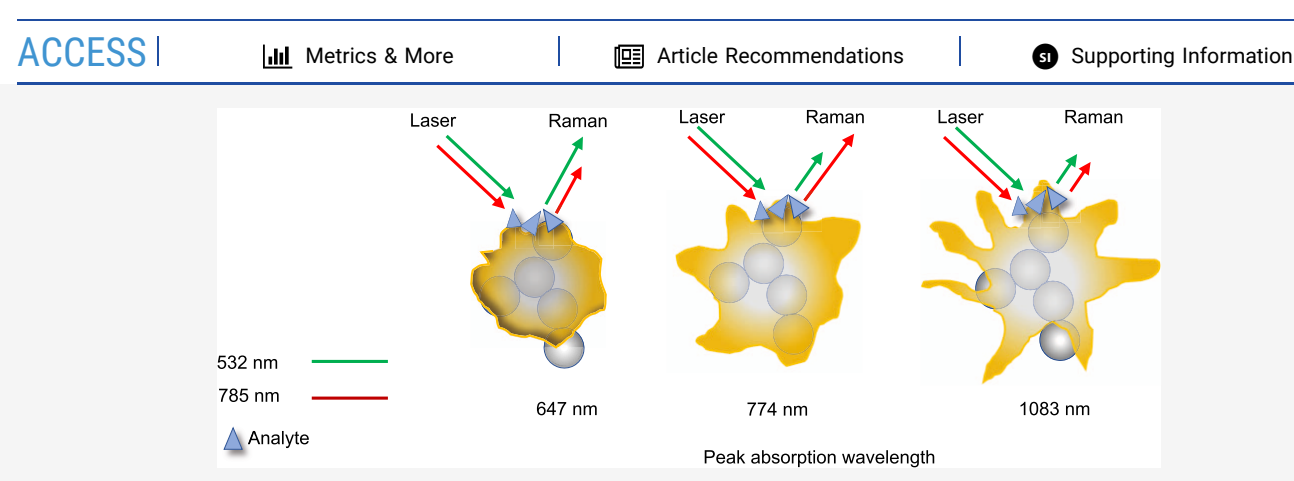
# LANGMUIR

pubs.acs.org/Langmuir Article

# Plasmon-Tuned Particles for the Amplification of Surface-Enhanced Raman Scattering from Analytes

Tania T. S. de Oliveira, Akram Abbasi, Irene Andreu, and Arijit Bose\*





ABSTRACT: Inelastic scattering from molecules because of vibrational modes produces unique Raman shifts, allowing these analytes to be detected with high specificity. Because Raman scattering is weak, surface-enhanced Raman scattering (SERS) has been used as a label-free technique for the detection of a variety of analytes at low concentrations. Using simple solution-based colloidal processing techniques, we have fabricated gold-coated carbon-black nanoparticles that show enhanced Raman activity. By varying the fabrication conditions, we create particles of different surface morphologies, allowing control over the peak wavelength for localized surface plasmon resonance (LSPR). By matching the LSPR wavelength to the incident laser wavelength, we get the highest signal from two model analytes, 4-nitrobenzenethiol (4-NBT) and Congo Red (CR). Our straightforward room-temperature-solution-based approach for making tunable SERS-active particles expands the range of incident radiation wavelengths that can be used for the detection of analytes using Raman scattering.

# 1. INTRODUCTION

Raman scattering arising from vibrational modes in analytes (often referred to as molecular Raman scattering) provides unique fingerprints allowing detection with great specificity. Because Raman signals are extremely weak, various strategies are used to overcome this limitation. In surface-enhanced Raman scattering (SERS), incident radiation excites surface plasmons on a rough metal substrate placed adjacent to a dielectric medium. The amplification of the incident electric field at the substrate surface enhances the Raman scattered signal, and a variety of analytes can be detected at low concentrations. <sup>2,5,6</sup>

Tuning the plasmon resonance of the SERS particles to the incident radiation wavelength can further enhance the local electric field in the vicinity of the substrate. The size and surface morphology of metal nanostructures can produce changes in their localized surface plasmon resonance (LSPR) wavelengths, suggesting a pathway for tuning the absorption characteristics of the particles. The shape of gold nanoparticles used for SERS has been varied by changing the concentrations of the gold salt, the reducing agent, or the seed particles. Gold nanospheres, aggregates of these

nanospheres, nanotriangles, and nanostars have been explored for the SERS-based detection of rhodamine 6G. The starshaped particles showed the maximum enhancement of SERS signals <sup>16</sup> because of the high enhancement of the electric fields at the tips. <sup>8,15,17–20</sup>

Gold-coated carbon-black nanoparticles (AuCB NPs) were developed previously for the detection of a variety of analytes using SERS.<sup>21</sup> In this work, we demonstrate a facile synthesis method in which the surface topology of the AuCB NPs is tuned by varying the concentration of an amine-containing polyelectrolyte that serves as a shape-directing agent. Carboxylterminated carbon-black particles serve as the underlying template, promoting the absorption of the polyelectrolyte as well as providing a morphological guide. The ability to fine-

Received: September 6, 2022 Revised: October 28, 2022 Published: November 9, 2022





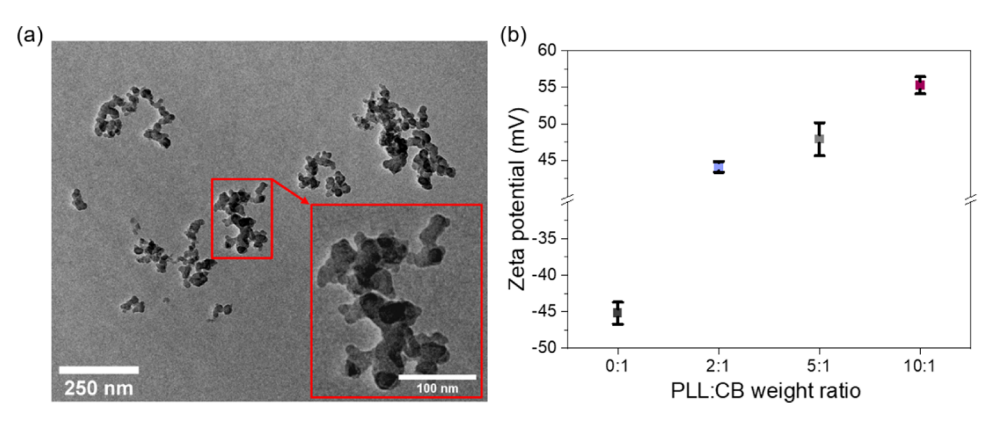


Figure 1. Characterization of CB particles: (a) TEM image of CB particles; (b)  $\zeta$ -potential of the CB and CB particles after the addition of PLL at pH 8. The error bars refer to the standard deviation of the measurements. Four different samples were used, and the measurements were done in duplicate.

tune the shape of our particles allows us to readily adjust the AuCB NP LSPR to match available laser excitation wavelengths, thus providing substantially increased SERS signals from a range of analytes.

Using 4-nitrobenzenethiol (4-NBT) and Congo Red (CR) as model analytes, we show that the strongest Raman signals arise when the laser wavelength, 532 and 785 nm for this study, is as close as possible to the LSPR wavelength of the particles. We note that this strategy is different from the resonance Raman Scattering, where the radiation energy is specifically matched to the energy transitions of the analyte.

To reduce the effects of heterogeneous hotspot distribution in our samples, we explored two commonly used SERS signal normalization methods: the electronic Raman scattering (ERS) signal from the gold on our particles and the signal from the underlying silicon substrate. Electronic Raman scattering arises from inelastic scattering from sp-band electrons in metals. The ERS signal appears in the low Raman shift region. For our particles, the magnitude and variability of the ERS and silicon signals were highly dependent on the incident laser wavelength. Both normalizations reduced the variability of the molecular Raman scattering signal for the 785 nm radiation, but not for the 532 nm radiation.

# 2. MATERIALS AND METHODS

Poly (L-lysine hydrochloride) (PLL, MW = 15,000–30,000), tetrachloroauric(III) acid trihydrate (HAuCl<sub>4</sub>·3H<sub>2</sub>O), 4-nitrobenzenethiol (4-NBT), 4-aminothiophenol (4-ATP), Congo Red (CR), and ascorbic acid (AA) were purchased from Sigma-Aldrich. Deionized water (DIW), with a resistance of 18 M $\Omega$ , was obtained from a Millipore Direct-3Q purification system. A para-aminobenzoic acid terminated carbon-black (CB) suspension (15% w/w) in water was obtained from Cabot Corporation. All materials were used as received.

**2.1.** Synthesis and Characterization of Gold-Coated Carbon-Black Particle (AuCB). Three different sets of particles were synthesized at room temperature with different PLL/CB weight ratios. We prepared 4 mL of aqueous PLL solutions at concentrations of 75, 175, and 375  $\mu$ g/mL. 1 mL of CB 0.015% w/w was added dropwise to the stirring PLL solution. The PLL/CB weight ratios for AuCB-A, AuCB-B, and AuCB-C particles were 2:1, 5:1, and 10:1, respectively. Subsequently, 1 mL of the suspension containing PLL and CB was added to 3 mL of DIW and mixed with 80  $\mu$ L of 50 mM HAuCl<sub>4</sub>, followed by the addition of 80  $\mu$ L of 75 mM ascorbic acid. The solution was stirred for 2 min and the appearance of a brownbluish color indicated the formation of AuCB nanoparticles. The suspension was centrifuged twice at 4930 g for 10 min, the supernatant was removed each time, and then the pellet was

resuspended in 4 mL of DIW. The sample suspensions were stored at 4  $^{\circ}\mathrm{C}$  until used.

The particles were imaged using transmission electron microscopy (TEM) on JEOL JEM-2100 at an accelerating voltage of 200 kV. Images were processed using ImageJ. For scanning transmission electron microscopy coupled with electron energy loss spectroscopy (STEM-EELS), a JEOL F200 STEM microscope equipped with a Gatan Continuum spectrometer was used. The STEM-EELS maps were acquired with a 1 nm per pixel spatial resolution and 50 meV/ch EELS energy dispersion. A Zeiss Sigma VP field emission scanning electron microscope was used to image the particles on silicon wafers. The extinction spectrum of the suspension was monitored using a Jasco spectrophotometer. A quartz cuvette was loaded with the AuCB NP diluted by a factor of 7 from the original suspension concentration. Optical densities were normalized by the highest value obtained in each extinction spectrum. A Malvern Zetasizer Nano ZS was used to determine the zeta potentials of the CB, PLLCB, and AuCB nanoparticles. A Brookhaven Instruments BI-2000SM goniometer was used to measure the hydrodynamic diameter of the nanoparticles at a scattering angle of 90°.

**2.2. Sample Preparation for Raman Scattering.** *2.2.1. 4-Nitrobenzenethiol* (*4-NBT*). AuCB nanoparticle pellets were resuspended in 3  $\mu$ L of an aqueous solution of 10  $\mu$ M 4-NBT in an ice bath while shaking for 24 h at 60 RPM to allow the analyte to be adsorbed on the particles. Excess 4-NBT was removed using three centrifugation washes with DIW. 30  $\mu$ L of the analyte-coated particle suspension was then deposited on a 5  $\times$  5 mm<sup>2</sup> plasmacleaned silicon wafer. The suspension spread uniformly over the wafer and was allowed to dry overnight at room temperature. These particle-loaded wafers were examined using confocal Raman microscopy and scanning electron microscopy.

2.2.2. Congo Red (CR). Because AuCB NPs and CR are oppositely charged, the addition of CR to the AuCB NP suspensions caused particle agglomeration and precipitation. Therefore, for these experiments, the AuCB NP suspension was deposited on a wafer and allowed to air dry overnight. Particle-coated silicon wafers were immersed in a 10  $\mu$ M aqueous CR solution overnight and then rinsed with DIW to remove unbound CR prior to Raman measurements.

Since ascorbic acid was added at the stoichiometric ratio, we assumed the complete reaction of all of the available HAuCl<sub>4</sub>. We used this information to make equal mass areal loadings of AuCB-A, AuCB-B, and AuCB-C on the silicon wafer for all our experiments, allowing us to compare signals from different particles.

2.2.3. Spectral Processing. A confocal Raman microscope (WITec  $\alpha$  300) with a 100× air objective and numerical aperture of 0.9 was used to probe our samples. A 785 nm 1.2 mW laser and a 532 nm 2.2 mW laser were used for incident radiation. The integration time was 15 s. For each substrate, 150 spectra were acquired in random spots. After baseline subtraction, all spectra were normalized by the laser power and integration time. <sup>24,25</sup> In an effort to reduce variability

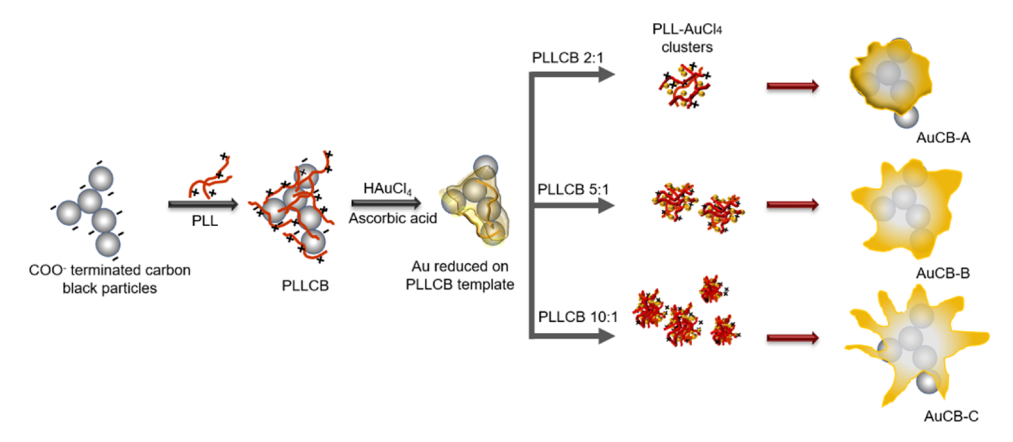


Figure 2. Proposed mechanism for the formation of AuCB particles. Varying the PLL concentration changes the number of PLL-AuCl<sub>4</sub> clusters. These clusters adsorb on the particles and act as nucleation sites. The different concentrations of nucleation sites result in different morphologies of AuCB-A, AuCB-B, and AuCB-C particles.

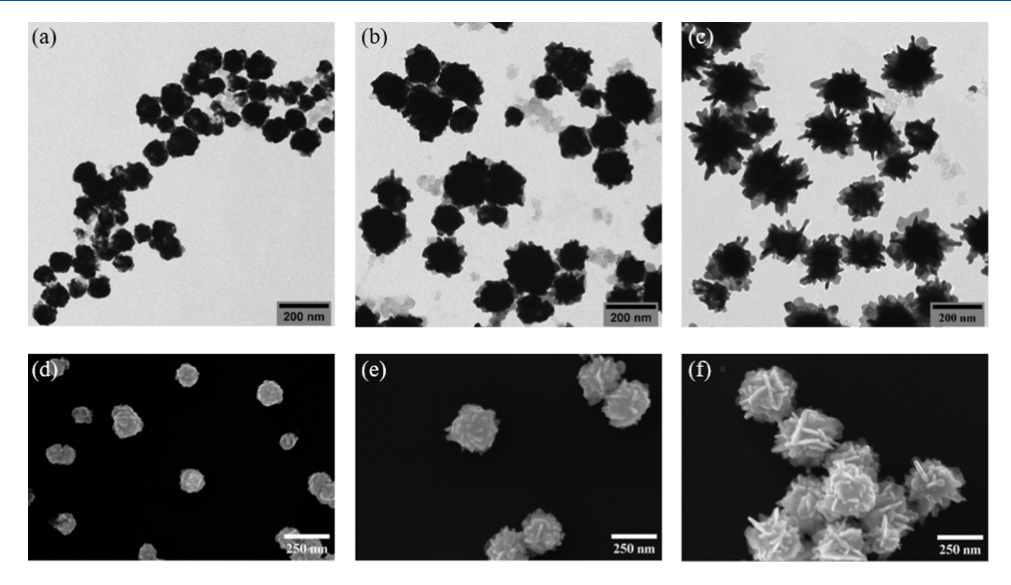


Figure 3. Images of AuCB synthesized with different PLL/CB weight ratios. TEM image of (a) AuCB-A, (b) AuCB-B, and (c) AuCB-C. SEM images of (d) AuCB-A, (e) AuCB-B, and (f) AuCB-C. TEM and SEM images show differences in the size and morphology of AuCB particles.

coming from random distributions of hotspots, Raman signals were also normalized using the electronic Raman scattering (ERS) from gold, <sup>22,26,27</sup> or by the signal coming from the underlying silicon wafer. <sup>28</sup> The ERS signals appear as pseduopeaks at a shift of 63 cm<sup>-1</sup> for the 785 nm laser and 108 cm<sup>-1</sup> for the 532 nm laser due to the presence of a long-pass filter to block Rayleigh scattering in our confocal Raman microscope. <sup>26</sup> The Raman peak from silicon was located at 523 cm<sup>-1</sup>. SERS measurements from 4-NBT on AuCB-A using a 633 nm laser excitation are shown in the Supporting Information.

## 3. RESULTS

**3.1. Carbon-Black Particle Characterization.** Figure 1a shows TEM images of the carbon-black nanoparticles used as templates for the synthesis of AuCB NP. The primary particle diameter is approximately 20 nm, and 8–10 of these particles fuse together forming random structures. The mean hydrodynamic diameter of the CB particles in aqueous suspension at 30  $\mu$ gm/L and pH 8 is 122  $\pm$  3 nm.

At pH 8, the carboxyl groups on the carbon-black particles are deprotonated and the  $\zeta$ -potential is  $-45 \pm 1.5$  mV (Figure 1b). PLL is a cationic polyelectrolyte, with repeating L-lysine units. It adsorbs on the negatively charged CB

particles, resulting in surface charge reversal as shown in Figure 1b. For PLL/CB weight ratios of 2:1, 5:1, and 10:1, the  $\zeta$ -potentials were +44  $\pm$  0.7, +48  $\pm$  2.3, and +55  $\pm$  1.2 mV, respectively, at pH  $\sim$ 8.

Carbon black in the AuCB can also induce nonspecific binding, potentially allowing probe molecules to remain close to the particle surfaces.<sup>21,32</sup>

**3.2. Poly**-L-Lysine Effect on AuCB Morphology. Particles AuCB-A, AuCB-B, and AuCB-C are formed by the process shown in Figure 2. Poly-L-lysine (PLL) is electrostatically attached to the surface of CB, reversing the  $\zeta$ -potential of CB particles from -45 mV to +55 mV. The HAuCl<sub>4</sub> solution is then added, and the AuCl<sub>4</sub><sup>-</sup> ions bind to the positively charged surface with some AuCl<sub>4</sub><sup>-</sup> ions remaining in the solution. The AuCl<sub>4</sub><sup>-</sup> ions on the particle surfaces as well as in the bulk solution are reduced to gold upon the addition of ascorbic acid. We hypothesize that PLL in the solution interacts with AuCl<sub>4</sub><sup>-</sup> ions, forming PLL-AuCl<sub>4</sub> clusters that adsorb on specific facets of the gold formed on the PLL/CB template, causing an anisotropic growth of AuCB NP. <sup>21,33-37</sup> Higher PLL concentrations increase the number of growth sites, leading to structures of different morphologies.

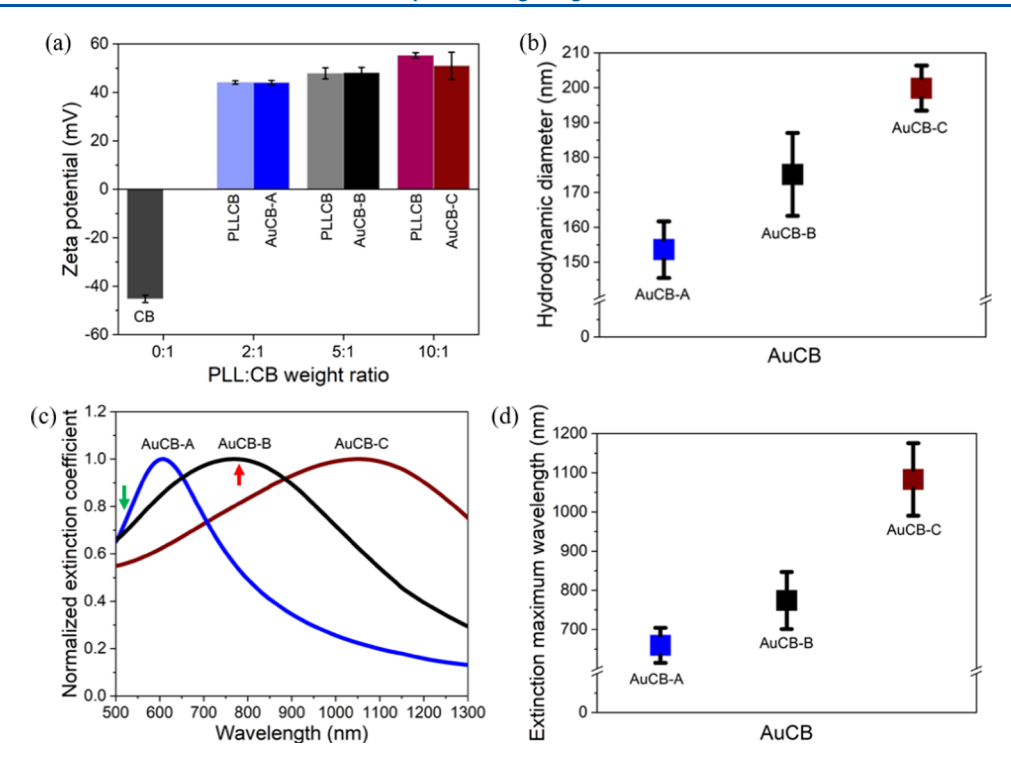


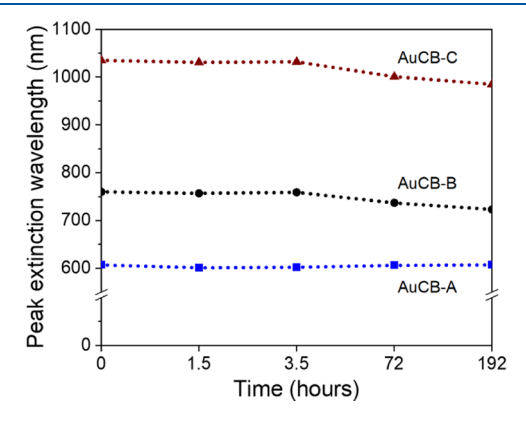
Figure 4. Characterization of the AuCB NP produced with different PLL/CB weight ratios. (a) ζ-Potentials of AuCB-A, AuCB-B, and AuCB-C. (b) Hydrodynamic diameters of particles AuCB-A, AuCB-B, and AuCB-C. (c) Extinction spectra of particles AuCB-A, AuCB-B, and AuCB-C averaged over nine independent samples. The green and red arrows show the laser wavelengths of 532 and 785 nm. The extinction spectra are broad because of the heterogeneity in the morphology of the nanostructures and differences in the size and morphology of the protrusions on the particle surfaces. (d) Average wavelength of the LSPR peak from nine separate samples. Error bars correspond to the standard deviation.

Figure 3a–c shows TEM images and Figure 3d–f shows SEM images of particles AuCB-A, AuCB-B, and AuCB-C. As the PLL/CB weight ratio increases, the particles show protrusions of increasing length, and their hydrodynamic diameters grow larger. The average height of these protrusions <sup>13,15</sup> are  $19 \pm 7$ ,  $38 \pm 12$ , and  $59 \pm 20$  nm for AuCB-A, AuCB-B, and AuCB-C, respectively.

Figure 4a shows the  $\zeta$ -potentials for PLL/CB with the different PLL-to-CB weight ratios and for AuCB-A, AuCB-B, and AuCB-C. Once PLL is adsorbed on the carbon-black particles, the  $\zeta$ -potential changes from negative to positive. Adsorption of AuCl<sub>4</sub><sup>-</sup> ions and a further reduction does not change the  $\zeta$ -potential, indicating that the charge on the particle surface is dominated by the charge on the cationic polyelectrolyte and HAuCl<sub>4</sub> is not in excess. The hydrodynamic diameters of AuCB-A, AuCB-B, and AuCB-C, shown in Figure 4b, are  $154 \pm 8$ ,  $175 \pm 12$ , and  $200 \pm 6$  nm, respectively. Figure 4c shows the extinction spectra averaged from nine separate samples for AuCB-A, AuCB-B, and AuCB-C. The spectra red-shift as well as broaden as the PLL/CB weight ratio is increased. The extinction spectra for AuCB NP dried on glass are shown in the Supporting Information (Figure S1). Figure 4d shows the location and average magnitude of the peak LSPR wavelength in the extinction spectrum of the nine samples. The broad extinction spectrum obtained from these particles is caused by the morphological heterogeneity of the underlying CB template, variations in particle size, and differences in the size, position, and shapes of the protrusions on the surface. 11,14,38,3

**3.3. Particle Stability.** We examined the stability of the suspensions containing AuCB-A, AuCB-B, and AuCB-C by monitoring the extinction spectra<sup>40</sup> over 8 days, as all analyte

detection experiments were performed within 1 week of synthesis of the particles. The location of the highest extinction peaks is shown in Figure 5. The wavelength of the extinction maximum remains essentially unchanged over 8 days, indicating that the particles do not change the morphology or aggregate over this period.<sup>40</sup>



**Figure 5.** Highest extinction peak monitored over time for AuCB-A, AuCB-B, and AuCB-C. *X*-axis scale logarithmic.

**3.4. SERS Measurements.** Since particles AuCB-A and AuCB-B had the nearest LSPR peak wavelengths to the available laser radiation of 785 and 532 nm, most of the Raman measurements were done with those two sets of particles.

We did electron energy loss spectroscopy (EELS) for our particles. <sup>41</sup> Figure 6 shows the maps for AuCB-A, AuCB-B, and AuCB-C. The energy windows correspond to surface plasmon modes with photon wavelengths ranging from 953 to 755 nm

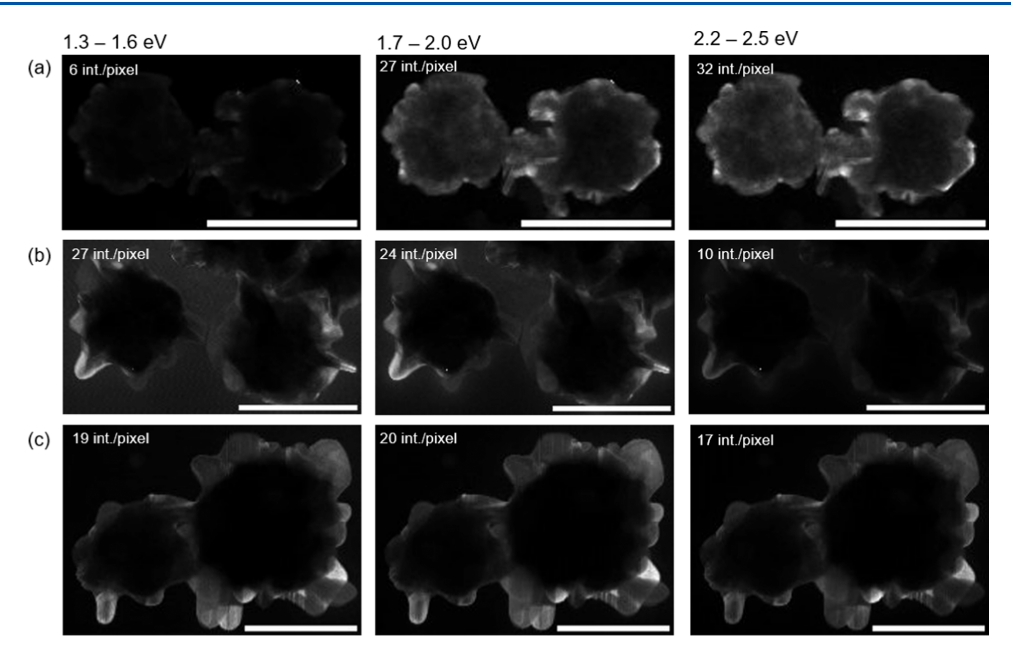


Figure 6. EELS maps showing plasmonic hotspots for AuCB-A, AuCB-B, and AuCB-C. The energy values shown correspond to surface plasmons modes with photon wavelengths of 953–755 nm (1.3–1.6 eV), 729–620 nm (1.7–2.0 eV), and 564–496 nm (2.2–2.5 eV). The number on the top left corner of each image is the average intensity per pixel. The scale bars are 100 nm.

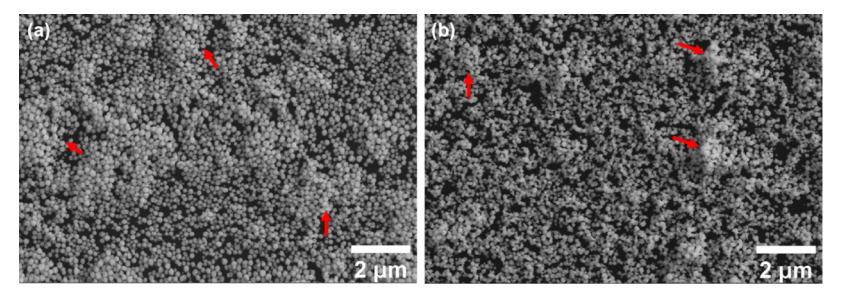


Figure 7. SEM images of dried films of (a) AuCB-A and (b) AuCB-B on plasma-cleaned silicon wafers. Drying introduces some agglomeration of the particles on the wafer, shown by red arrows.

(1.3–1.6 eV), 729 to 620 nm (1.7–2.0 eV), and 564 to 496 nm (2.2–2.5 eV). The average intensity of the pixels around the particle is noted on each map. The intensity of the plasmons of AuCB-A increases as the photon wavelength decreases, whereas the plasmon intensity of AuCB-B decreases as the photon wavelength decreases. AuCB-C EELS map intensities remain almost constant within the experimentally available photon energies, in agreement with the long-wavelength resonance energy. The maximum plasmon intensities are in the regions of the highest curvature of these particles. 42,43

Figure 7 shows SEM images of the particles on the wafer after drying. The particles are distributed over the silicon wafer surface, and there is some drying-related agglomeration. Raman signals from the 4-NBT and Congo Red coated samples were acquired on multiple spots on the substrate. The same substrates were used to acquire data for the 785 and 532 nm lasers.

While both 4-NBT and Congo Red show several signature Raman shifts that correspond to vibrations associated with different bonds in the molecules, we focus on the prominent  $NO_2$  symmetric stretch at 1337 cm<sup>-1</sup> for 4-NBT, <sup>44–46</sup> and the phenyl-N stretch at 1157 cm<sup>-1</sup> for the Congo Red. <sup>47</sup>Figure 8a,b show the data from the 785 and 532 nm lasers, respectively, and are the average of the 150 Raman spectra

gathered from different randomly selected spots on the substrates. For all of the spectra, the background was subtracted <sup>26</sup> and then normalized by laser power and integration time. <sup>25</sup>

Figure 8c,d shows the average intensities of the 1337 cm<sup>-1</sup> signal corresponding to the NO<sub>2</sub> symmetric stretch.<sup>44–46</sup> AuCB-B, with an LSPR maximum at 780 nm, produced the highest Raman signal intensity for the measurements with 785 nm laser excitation, and the AuCB-A with an LSPR maximum at 630 nm gave the highest Raman signal for the 532 nm excitation source. This result supports the hypothesis that the highest Raman signals come from excitation at wavelengths closest to the LSPR of the particles. 48-51 Raman spectra from 4-NBT on AuCB-A with a 633 nm wavelength laser are presented in the Supporting Information, Figure S2. The signals from AuCB-C were weaker than from the other two types of particles for both lasers, (Figure S3 in the Supporting Information). Additionally, 4-aminothiophenol (4-ATP) was also detected and showed the same trend as 4-NBT (Figure S4 in the Supporting Information).

These experiments were repeated for CR and shown in Figure 9a,b. AuCB-B gave a higher signal with the 785 nm laser excitation, while AuCB-A showed a higher signal for the 532 nm laser source. Figure 9c,d shows the intensity of the 1157 cm<sup>-1</sup> peaks from the phenyl-N stretch of the CR.<sup>47</sup> For this

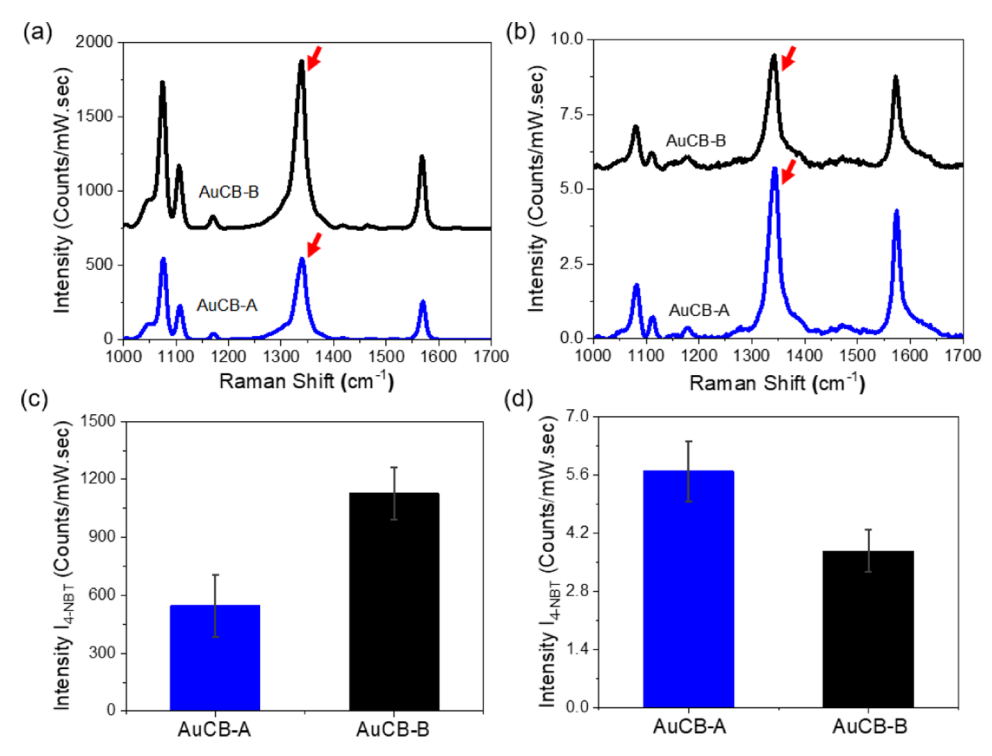


Figure 8. Raman spectra for the AuCB nanoparticles after exposure to a 10  $\mu$ M 4-NBT solution for (a) 785 nm excitation and (b) 532 nm excitation. The arrows in (a) and (b) point to the NO<sub>2</sub> symmetric stretch for 4-NBT at 1337 cm<sup>-1</sup>. The average and standard deviation of the intensity of the selected 4-NBT Raman peak ( $I_{4-NBT}$ ) for (c) 785 nm excitation and (d) 532 nm excitation. Error bars are the standard deviation from 150 spectra.

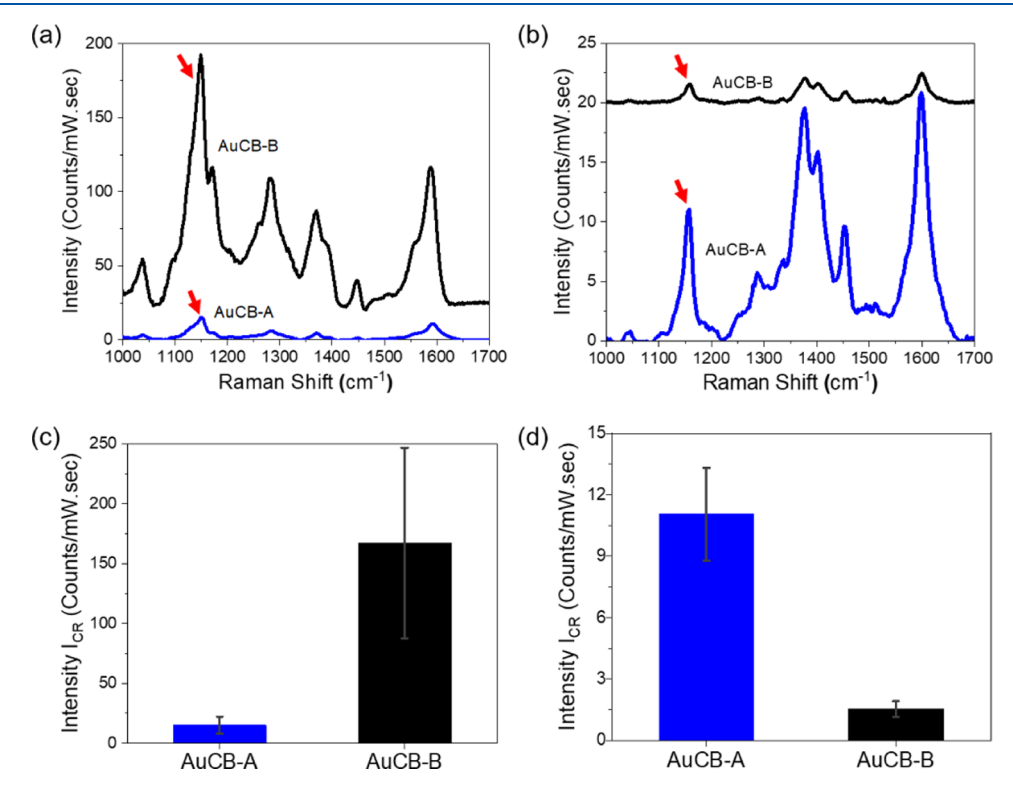


Figure 9. Raman spectra for AuCB nanoparticles after exposure to  $10 \,\mu\mathrm{M}$  Congo Red (CR) solution for (a) 785 nm laser excitation and (b) 532 nm laser excitation. The arrows in (a) and (b) point to the phenyl-N stretch at  $1157 \,\mathrm{cm}^{-1}$ . The average and standard deviation of the intensity of the selected Raman peak of CR ( $I_{CR}$ ) for (c) 785 nm excitation and (d) 532 nm excitation.

analyte too, the highest Raman signals arose when the laser wavelength was closest to the particle LSPR. The Raman spectra from CR are different for 532 and 785 nm wavelength

excitations because tCR exhibits an absorption band in the visible range from 398 to 580 nm with a maximum at 496 nm,

which is in resonance with a laser of 532 nm (Figure S5 in the Supporting Information).<sup>48,52</sup>

We calculated enhancement factors (EF) for our particles, defined by EF =  $\frac{I_{\text{Ausheet}}}{I_{\text{Ausheet}}}$ , where  $I_{\text{AuCB}}$  and  $I_{\text{Ausheet}}$  are the intensities of the Raman signals from the 1337 cm<sup>-1</sup> NO<sub>2</sub> symmetric stretch for 4-NBT on our AuCB NP and 4-NBT deposited on a gold sheet, respectively. Each signal is normalized by the integration time. The EF values, presented in Table 1, for the two excitation wavelengths used in this work are of the same order of magnitude as those shown by others.  $^{21,54-59}$ 

Table 1. Enhancement Factor for AuCB NPs

	laser wavelength (785 nm)	laser wavelength (532 nm)
particle	EF	EF
AuCB-A	$3.5 \times 10^4$	$6.9 \times 10^{2}$
AuCB-B	$7.3 \times 10^4$	$2.6 \times 10^{2}$
AuCB-C	$1.2 \times 10^4$	$2.4 \times 10^{2}$

We have demonstrated that our AuCB nanoparticles can be used to detect analytes via SERS, exploiting two different analyte—substrate interaction mechanisms, covalent bonds for thiolated analytes, and electrostatic interaction for negatively charged analytes. We have also demonstrated the versatility of AuCB, which can be mixed with samples of analyte in a suspension or deposited and dried first on a substrate and then exposed to the analyte solution.

**3.5.** Data Normalization Using Electronic Raman Scattering (ERS) and Silicon Signals. The long-pass filter used to block the Raleigh scatter truncates the ERS signals and creates pseudo-peaks at Raman shifts of 108 and 63 cm<sup>-1</sup> for the 785 and 532 nm radiation, respectively. The silicon shift is at 523 cm<sup>-1</sup>. Figure 10a,b shows the intensities of the ERS

pseudo-peaks,  $I_{\rm ERS}$ , and signal from the silicon,  $I_{\rm Si}$ , for the 785 nm radiation, and Figure 10c,d shows those intensities for the 532 nm radiation. The silicon signal is dependent on gaps in the coverage of the wafer by the particles and small differences in the thickness of the coating of AuCB on the silicon wafer. Because of the shorter penetration depth of the 532 nm radiation,  $I_{\rm Si}$  has a large variability for both AuCB-A and AuCB-B.

Therefore, we decided to only pursue normalization by the ERS pseudo-peak (data shown in Figure S6 in the Supporting Information).  $I_{\rm ERS}$  from the 785 nm excitation is of the order of 850 counts/mW·s with a low standard deviation, while that from the 532 nm excitation is of the order of 0.7 counts/mW·s with a large standard deviation. The differences in variability arise from the difference in the ERS signal intensity; while the ERS signal is much higher than the spectral noise for the 785 nm laser, the ERS signal intensity at 532 nm excitation is comparable to the spectral noise. The low Raman-shift ERS effect is enhanced with the near-infrared excitation compared to the visible-light excitation because the photons at the near-infrared wavelength do not have enough energy to excite interband and intraband transitions.  $^{22}$ 

As shown in Figure 11, normalization of the Raman signals using ERS ( $I_{4\text{-NBT}}/I_{\text{ERS}}$ ) at 532 nm does not result in reduced variability, while it did reduce variability for the 785 nm laser going from a coefficient of variation of 29 to 5% for AuCB-A and a coefficient of variation going from 12 to 8% for AuCB-B. Therefore, using nanoparticles optimized for 785 nm excitation and normalizing the data using the ERS peak to account for the variability of hotspot distribution has the potential to improve reproducibility and lower the detection limit for analytes.

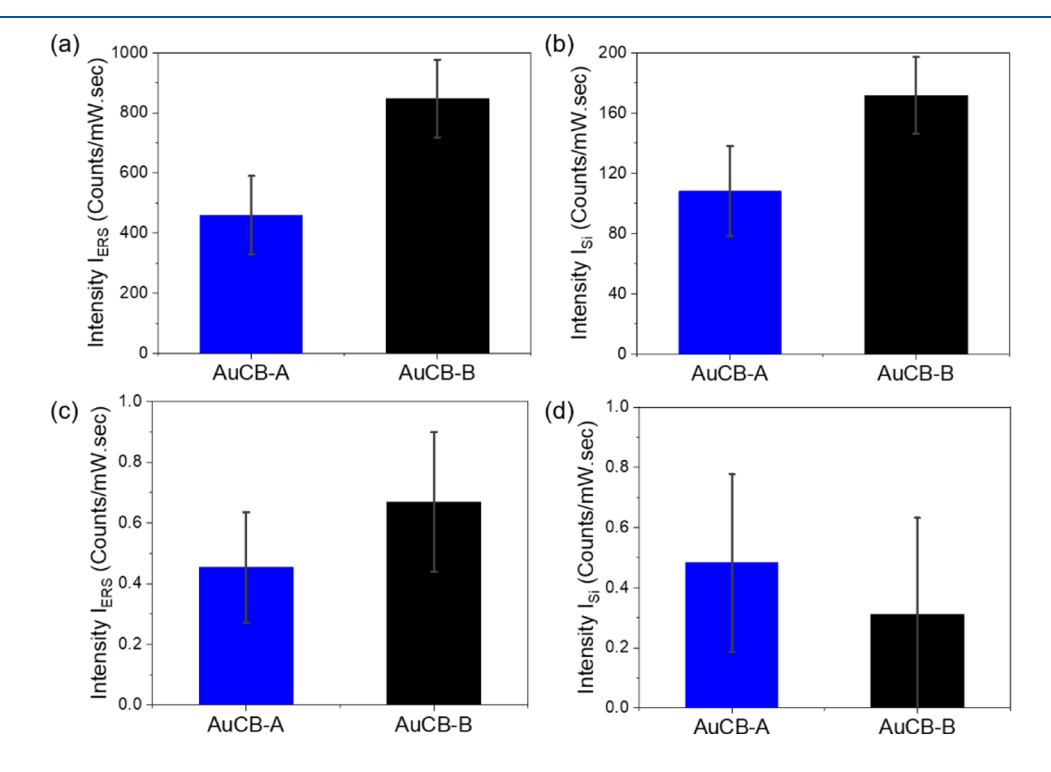


Figure 10. Intensity of the ERS ( $I_{ERS}$ ) and Si ( $I_{Si}$ ) wafer signals for particles AuCB-A, and AuCB-B. (a)  $I_{ERS}$  (b) and  $I_{Si}$  for 785 nm laser source. (c)  $I_{ERS}$  and (d)  $I_{Si}$  for 532 nm laser source.

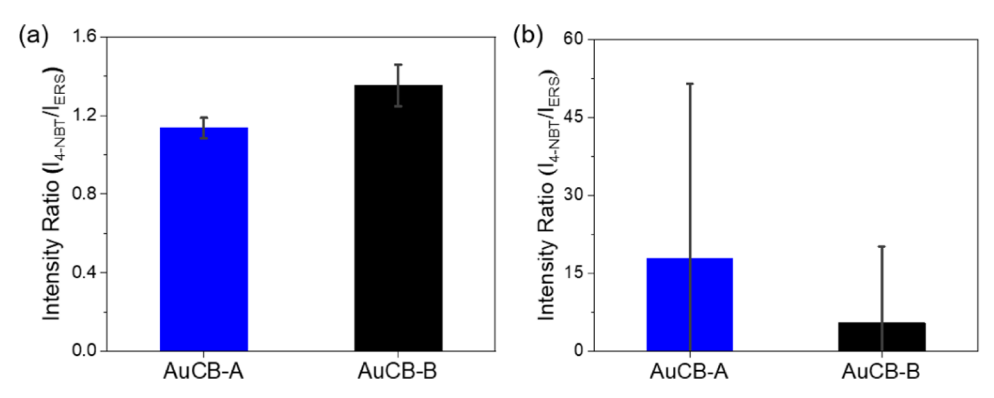


Figure 11. Intensity ratios from normalization with the electronic Raman scattering signal: (a) 785 nm laser and (b) 532 nm laser for AuCB particles exposed to 4-NBT. Error bars are the standard deviation of 150 measurements.

# 4. CONCLUSIONS

Gold-coated carbon-black particles were synthesized using colloidal processing at room temperature. Varying the concentration of the cationic polyelectrolyte coated on the anionic carbon-black particles allows tuning the size and morphology of the particles and thus the peak localized surface plasmon resonance wavelength (LSPR). When the LSPR of the nanoparticles is most closely matched to the incident laser wavelength, the Raman signals from two analytes with distinct substrate attachment mechanisms showed the greatest intensity. For the two hotspot normalization methods evaluated, ERS normalization of the data acquired with a 785 nm laser excitation showed the best reduction in signal variability.

## ASSOCIATED CONTENT

#### **Supporting Information**

The Supporting Information is available free of charge at https://pubs.acs.org/doi/10.1021/acs.langmuir.2c02451.

Extinction spectra of particles on glass slides; SERS spectra of 4-NBT and CR on AuCB-C; SERS spectra of 4-NBT on AuCB-A at 532 and 633 nm; SERS spectra of 4-ATP on AuCB; extinction spectra of CR; and Raman spectra showing the ERS peak for 532 and 785 nm wavelengths (PDF)

# AUTHOR INFORMATION

# **Corresponding Author**

Arijit Bose — Department of Chemical Engineering, University of Rhode Island, Kingston, Rhode Island 02881, United States; orcid.org/0000-0002-2309-5087; Phone: (401) 874-2804; Email: bosea@uri.edu

#### **Authors**

Tania T. S. de Oliveira – Department of Chemical Engineering, University of Rhode Island, Kingston, Rhode Island 02881, United States

Akram Abbasi — School of Engineering, Center for Biomedical Engineering, Brown University, Providence, Rhode Island 02912, United States; orcid.org/0000-0003-2877-8204

Irene Andreu — Department of Chemical Engineering, University of Rhode Island, Kingston, Rhode Island 02881, United States; orcid.org/0000-0001-7689-2269

Complete contact information is available at: https://pubs.acs.org/10.1021/acs.langmuir.2c02451

#### Notes

The authors declare no competing financial interest.

#### ACKNOWLEDGMENTS

This work is based upon work supported in part by the National Science Foundation under EPSCoR Cooperative Agreement OIA-1655221. The TEM, SEM, and Raman data were acquired at the RI Consortium for Nanoscience and Nanotechnology, a URI College of Engineering core facility partially funded by the National Science Foundation EPSCoR, Cooperative Agreement #OIA-1655221, and #CBET-1919588. The Raman data with a 633 nm excitation was obtained at the Instrumentation for Molecular and Nanoscience Innovation facility at Brown University.

#### REFERENCES

- (1) Albrecht, A. C. On the Theory of Raman Intensities. *J. Chem. Phys.* **1961**, 34, 1476–1484.
- (2) Langer, J.; de Aberasturi, D. J.; Aizpurua, J.; Alvarez-Puebla, R. A.; Auguié, B.; Baumberg, J. J.; Bazan, G. C.; Bell, S. E. J.; Boisen, A.; Brolo, A. G.; Choo, J.; Cialla-May, D.; Deckert, V.; Fabris, L.; Faulds, K.; de Abajo, F. J. G.; Goodacre, R.; Graham, D.; Haes, A. J.; Haynes, C. L.; Huck, C.; Itoh, T.; Käll, M.; Kneipp, J.; Kotov, N. A.; Kuang, H.; Ru, E. C. L.; Lee, H. K.; Li, J. F.; Ling, X. Y.; Maier, S. A.; Mayerhöfer, T.; Moskovits, M.; Murakoshi, K.; Nam, J. M.; Nie, S.; Ozaki, Y.; Pastoriza-Santos, I.; Perez-Juste, J.; Popp, J.; Pucci, A.; Reich, S.; Ren, B.; Schatz, G. C.; Shegai, T.; Schlücker, S.; Tay, L. L.; Thomas, K. G.; Tian, Z. Q.; Van Duyne, R. P.; Vo-Dinh, T.; Wang, Y.; Willets, K. A.; Xu, C.; Xu, H.; Xu, Y.; Yamamoto, Y. S.; Zhao, B.; Liz-Marzán, L. M. Present and Future of Surface-Enhanced Raman Scattering. ACS Nano 2020, 14, 28–117.
- (3) Mcnay, G.; Eustace, D.; Smith, W. E.; Faulds, K.; Graham, D. Focal point review Surface-Enhanced Raman Scattering (SERS) and Surface-Enhanced Resonance Raman Scattering (SERRS): A Review of Applications. *Appl. Spectrosc.* **2011**, *65*, 825–837.
- (4) Mosier-Boss, P. A. Review of SERS Substrates for Chemical Sensing. *Nanomaterials* **2017**, *7*, No. 142.
- (5) Kneipp, K.; Wang, Y.; Kneipp, H.; Perelman, L. T.; Itzkan, I.; Dasari, R. R.; Feld, M. S. Single Molecule Detection Using Surface-Enhanced Raman Scattering. *Phys. Rev. Lett.* **1997**, *9*, 1667–1670.
- (6) Pilot, R.; Signorini, R.; Durante, C.; Orian, L.; Bhamidipati, M.; Fabris, L. A Review on Surface-Enhanced Raman Scattering. *Biosensors* **2019**, *9*, No. 57.
- (7) Wang, H.; Pu, Y.; Shan, B.; Li, M. Combining Experiments and Theoretical Modeling To Interrogate the Anisotropic Growth and Structure-Plasmonic Property Relationships of Gold Nanostars. *Inorg. Chem.* **2019**, *58*, 12457–12466.
- (8) Barbosa, S.; Agrawal, A.; Rodriguez-Lorenzo, L.; Pastoriza-Santos, I.; Alvarez-Puebla, R. A.; Kornowski, A.; Weller, H.; Liz-

- Marzan, L. M. Tuning size and sensing properties in colloidal gold nanostars. *Langmuir* **2010**, *26*, 14943–14950.
- (9) Han, B.; Chen, L.; Jin, S.; Guo, S.; Park, J.; Yoo, H. S.; Park, J. H.; Zhao, B.; Jung, Y. M. Modulating Mechanism of the LSPR and SERS in Ag/ITO Film: Carrier Density Effect. *J. Phys. Chem. Lett.* **2021**, *12*, 7612–7618.
- (10) Mahajan, S.; Abdelsalam, M.; Suguwara, Y.; Cintra, S.; Russell, A.; Baumberg, J.; Bartlett, P. Tuning plasmons on nano-structured substrates for NIR-SERS. *Phys. Chem. Chem. Phys.* **2007**, *9*, 104–109.
- (11) Li, J.; Wu, J.; Zhang, X.; Liu, Y.; Zhou, D.; Sun, H.; Zhang, H.; Yang, B. Controllable Synthesis of Stable Urchin-like Gold Nanoparticles Using Hydroquinone to Tune the Reactivity of Gold Chloride. J. Phys. Chem. C 2011, 115, 3630–3637.
- (12) Chandra, K.; Culver, K. S. B.; Werner, S. E.; Lee, R. C.; Odom, T. W. Manipulating the Anisotropic Structure of Gold Nanostars using Good's Buffers. *Chem. Mater.* **2016**, *28*, 6763–6769.
- (13) Pu, Y.; Zhao, Y.; Zheng, P.; Li, M. Elucidating the Growth Mechanism of Plasmonic Gold Nanostars with Tunable Optical and Photothermal Properties. *Inorg. Chem.* **2018**, *57*, 8599–8607.
- (14) Ahmed, W.; Kooij, E. S.; van Silfhout, A.; Poelsema, B. Controlling the morphology of multi-branched gold nanoparticles. *Nanotechnology* **2010**, *21*, No. 125605.
- (15) Khoury, C. G.; Vo-Dinh, T. Gold Nanostars For Surface-Enhanced Raman Scattering Synthesis, Characterization and Optimization. *J. Phys. Chem. C* 2008, *112*, 18849–18859.
- (16) Tian, F.; Bonnier, F.; Casey, A.; Shanahan, A. E.; Byrne, H. J. Surface enhanced Raman scattering with gold nanoparticles: effect of particle shape. *Anal. Methods* **2014**, *6*, 9116–9123.
- (17) Yuan, H.; Khoury, C. G.; Hwang, H.; Wilson, C. M.; Grant, G. A.; Vo-Dinh, T. Gold nanostars: surfactant-free synthesis,3D modelling, and two-photonphotoluminescence imaging. *Nanotechnology* **2012**, 23, No. 075102.
- (18) Reguera, J.; Langer, J.; de Aberasturiab, D. J.; Liz-Marzán, L. M. Anisotropic metal nanoparticles for surfaceenhanced Raman scattering. *Chem. Soc. Rev.* **2017**, *46*, 3866–3885.
- (19) Meng, X.; Dyer, J.; Huo, Y.; Jiang, C. Greater SERS Activity of Ligand-Stabilized Gold Nanostars withSharp Branches. *Langmuir* **2020**, *36*, 3558–3564.
- (20) Rodriguez-Lorenzo, L.; Alvarez-Puebla, R. A.; de Abajo, F. J. G.; Liz-Marzán, L. M. Surface Enhanced Raman Scattering Using Star-Shaped Gold Colloidal Nanoparticles. *J. Phys. Chem. C* **2010**, *114*, 7336–7340.
- (21) Abbasi, A.; de Oliveira, T. T. S.; Bothun, G. D.; Bose, A. Carbon Black Templated Gold Nanoparticles for Detection of a Broad Spectrum of Analytes by Surface-Enhanced Raman Scattering. ACS Appl. Nano Mater. 2020, 3, 2605–2613.
- (22) Nam, W.; Zhao, Y.; Song, J.; Tali, S. A. S.; Kang, S.; Zhu, W.; Lezec, H. J.; Agrawal, A.; Vikesland, P. J.; Zhou, W. Plasmonic Electronic Raman Scattering as Internal Standard for Spatial and Temporal Calibration in Quantitative Surface-Enhanced Raman Spectroscopy. J. Phys. Chem. Lett. 2020, 11, 9543–9551.
- (23) Xue, Y.; Li, X.; Li, H.; Zhang, W. Quantifying thiol-gold interactions towards the efficient strength control. *Nat. Commun.* **2014**, *5*, No. 4348.
- (24) Gautam, R.; Vanga, S.; Ariese, F.; Umapathy, S. Review of multidimensional dataprocessing approaches for Raman andinfrared spectroscopy. *EPI Tech. Instrum.* **2015**, *2*, No. 8.
- (25) Karawdeniya, B. I.; Chevalier, R. B.; Bandara, Y. M. N. D. Y.; Dwyer, J. R. Targeting improved reproducibility in surface-enhanced Raman spectroscopy with planar substrates using 3D printed alignment holders. *Rev. Sci. Instrum.* **2021**, *92*, No. 043102.
- (26) Wei, H.; Leng, W.; Song, J.; Willner, M. R.; Marr, L. C.; Zhou, W.; Vikesland, P. J. Improved Quantitative SERS Enabled by Surface Plasmon Enhanced Elastic Light Scattering. *Anal. Chem.* **2018**, *90*, 3227–3237.
- (27) Wei, H.; McCarthy, A.; Song, J.; Zhou, W.; Vikesland, P. J. Quantitative SERS by hot spot normalization surface enhanced Rayleigh band intensity as an alternative evaluation parameter for SERS substrate performance. *Faraday Discuss.* **2017**, 205, 491–504.

- (28) Fu, H.; Bao, H.; Zhang, H.; Zhao, Q.; Zhou, L.; Zhu, S.; Wei, Y.; Li, Y.; Cai, W. Quantitative Surface-Enhanced Raman Spectroscopy for Field Detections Based on Structurally Homogeneous Silver-Coated Silicon Nanocone Arrays. ACS Omega 2021, 6, 18928–18938.
- (29) Katepalli, H.; John, V. T.; Bose, A. The response of carbon black stabilized oil-in-water emulsions to the addition of surfactant solutions. *Langmuir* **2013**, *29*, 6790–6797.
- (30) Guo, Y.; Ma, Y.; Xu, L.; Li, J.; Yang, W. Conformational Change Induced Reversible/Assembly Disassembly of Poly-L-Lysine-Functionalized Gold Nanoparticles. *J. Phys. Chem. C* **2007**, *111*, 9172–9176.
- (31) Koenig, J. L.; Sutton, L. P. Raman Spectra of Poly-L-Lysines. *Biopolymers* 1970, 9, 1229–1237.
- (32) Baik, S. Y.; Cho, Y. J.; Lim, Y. R.; Im, H. S.; Jang, D. M.; Myung, Y.; Park, J.; Kang, H. S. Charge-Selective Surface-Enhanced Raman Scattering Using Silver and Gold Nanoparticles Deposited on Silicon—Carbon Core—Shell Nanowires. *ACS Nano* **2012**, *3*, 2459—2470
- (33) Chen, M.; Wu, B.; Yang, J.; Zheng, N. Small adsorbate-assisted shape control of Pd and Pt nanocrystals. *Adv. Mater.* **2012**, *24*, 862–879
- (34) Fu, G. T.; Jiang, X.; Wu, R.; Wei, S. H.; Sun, D. M.; Tang, Y. W.; Lu, T. H.; Chen, Y. Arginine-assisted synthesis and catalytic properties of single-crystalline palladium tetrapods. *ACS Appl. Mater. Interfaces* **2014**, *6*, 22790–22795.
- (35) Pan, A.; Jakaria, M. G.; Meenach, S. A.; Bothun, G. D. Radiofrequency and Near-Infrared Responsive Core-ShellNanostructures Using Layersome Templates for Cancer Treatment. *ACS Appl. Bio Mater.* **2020**, *3*, 273–281.
- (36) Plascencia-Villa, G.; Torrente, D.; Marucho, M.; Jose-Yacaman, M. Biodirected synthesis and nanostructural characterization of anisotropic gold nanoparticles. *Langmuir* **2015**, *31*, 3527–3536.
- (37) Zhong, Z.; Patskovskyy, S.; Bouvrette, P.; Luong, J. H. T.; Gedanken, A. The Surface Chemistry of Au Colloids and Their Interactions with Functional Amino Acids. *J. Phys. Chem. B* **2004**, *108*, 4046–4052.
- (38) Hao, E.; Bailey, R. C.; Schatz, G. C.; Hupp, J. T.; Li, S. Synthesis and Optical Properties of "Branched" Gold Nanocrystals. *Nano Lett.* **2004**, *4*, 327–330.
- (39) Yu, X.; Zhong, Y.; Sun, Y.; Chen, Y. Controllable Preparation of Plasmonic Gold Nanostars for Enhanced Photothermal and SERS Effects. *Chem. Res. Chin. Univ.* **2020**, *36*, 1284–1291.
- (40) Bakr, O. M.; Wunsch, B. H.; Stellacci, F. High-Yield Synthesis of Multi-Branched Urchin-Like GoldNanoparticles. *Chem. Mater.* **2006**, *18*, 3297–3301.
- (41) Wu, Y.; Li, G.; Camden, J. P. Probing Nanoparticle Plasmons with Electron Energy Loss Spectroscopy. *Chem. Rev.* **2018**, *118*, 2994–3031.
- (42) Lin, W. H.; Lu, Y. H.; Hsu, Y. J. Au nanoplates as robust, recyclable SERS substrates for ultrasensitive chemical sensing. *J. Colloid Interface Sci.* **2014**, *418*, 87–94.
- (43) Song, C. Y.; Zhou, N.; Yang, B. Y.; Yang, Y. J.; Wang, L. H. Facile synthesis of hydrangea flower-like hierarchical gold nanostructures with tunable surface topographies for single-particle surface-enhanced Raman scattering. *Nanoscale* **2015**, *7*, 17004–17011.
- (44) Juergensen, S.; Kusch, P.; Reich, S. Resonant Raman Scattering of 4-Nitrothiophenol. *Phys. Status Solidi B* **2020**, 257, No. 2000295.
- (45) Abdelsalam, M. Surface enhanced raman scattering of aromatic thiols adsorbed on nanostructured gold surfaces. *Open Chem.* **2009**, *7*, 446–453.
- (46) Kim, K.; Shin, D.; Lee, H. B.; Shin, K. S. Surface-enhanced Raman scattering of 4-aminobenzenethiol on gold: the concept of threshold energy in charge transfer enhancement. *Chem. Commun.* **2011**, *47*, 2020–2022.
- (47) Bonancêa, C. E.; do Nascimento, G. M.; de Souza, M. L.; Temperini, M. L. A.; Corio, P. Substrate development for surface-enhanced Raman study of photocatalytic degradation processes: Congo red over silver modified titanium dioxide films. *Appl. Catal., B* **2006**, *69*, 34–42.

- (48) Álvarez-Puebla, R. A. Effects of the Excitation Wavelength on the SERS Spectrum. J. Phys. Chem. Lett. 2012, 3, 857–866.
- (49) Johnson, B. B.; Peticolas, W. L. The Resonant Raman Effect. Annu. Rev. Phys. Chem. 1976, 27, 465-491.
- (50) Robert, B. Resonance Raman spectroscopy. *Photosynth. Res.* 2009, 101, 147-155.
- (51) Willets, K. A.; Van Duyne, R. P. Localized surface plasmon resonance spectroscopy and sensing. *Annu. Rev. Phys. Chem.* **2007**, 58, 267–297.
- (52) Lee, J.; Yoo, J.; Kim, J.; Jang, Y.; Shin, K.; Ha, E.; Ryu, S.; Kim, B.-G.; Wooh, S.; Char, K. Development of Multimodal Antibacterial Surfaces Using PorousAmine-Reactive Films Incorporating Lubricant and SilverNanoparticles. ACS Appl. Mater. Interfaces 2019, 11, 6550–6560.
- (53) Pavel, I. E.; Alnajjar, K. S.; Monahan, J. L.; Stahler, A.; Hunter, N. E.; Weaver, K. M.; Baker, J. D.; Meyerhoefer, A. J.; Dolson, D. A. Estimating the Analytical and Surface Enhancement Factorsin Surface-Enhanced Raman Scattering (SERS): A Novel PhysicalChemistry and Nanotechnology Laboratory Experiment. J. Chem. Educ. 2012, 89, 286–290.
- (54) Chen, J.; Huang, Y.; Kannan, P.; Zhang, L.; Lin, Z.; Zhang, J.; Chen, T.; Guo, L. Flexible and Adhesive Surface Enhance Raman Scattering Active Tape for Rapid Detection of Pesticide Residues in Fruits and Vegetables. *Anal. Chem.* **2016**, *88*, 2149–2155.
- (55) Dai, L.; Song, L.; Huang, Y.; Zhang, L.; Lu, X.; Zhang, J.; Chen, T. Bimetallic Au/Ag Core—Shell Superstructures with Tunable Surface Plasmon Resonance in the Near-Infrared Region and High Performance Surface-Enhanced Raman Scattering. *Langmuir* **2017**, 33, 5378—5384.
- (56) Le Ru, E. C.; Blackie, E.; Meyer, M.; Etchegoin, P. G. Surface Enhanced Raman Scattering Enhancement Factors: A Comprehensive Study. *J. Phys. Chem. C* **2007**, *111*, 13794–13803.
- (57) Lu, X.; Huang, Y.; Liu, B.; Zhang, L.; Song, L.; Zhang, J.; Zhang, A.; Chen, T. Light-Controlled Shrinkage of Large-Area Gold Nanoparticle Monolayer Film for Tunable SERS Activity. *Chem. Mater.* **2018**, *30*, 1989–1997.
- (58) Song, L.; Huang, Y.; Nie, Z.; Chen, T. Macroscopic twodimensional monolayer films of gold nanoparticles: fabrication strategies, surface engineering and functional applications. *Nanoscale* **2020**, *12*, 7433–7460.
- (59) Haynes, C. L.; McFarland, A. D.; Duyne, R. P. V. Surface-Enhacement Raman Spectoscopy. *Anal. Chem.* **2005**, 339–345.